

Development of a compact alpha and beta  
camera for dismantlement applications

Sylvain Leblond<sup>a\*</sup>, Pascal Fichet<sup>a</sup>, Rémi Laumonier<sup>b</sup>, Sophie Billon<sup>c</sup>,  
Paul Sardini<sup>c</sup>, Kimberly Colas<sup>a</sup>

<sup>a</sup>Université Paris-Saclay, CEA, Service d'Études Analytiques et de Réactivité des Surfaces,  
91191, Gif-sur-Yvette, France.

\* current affiliation : Université Paris-Saclay, CEA, List, Laboratoire National Henri Becquerel (LNE-LNHB), F-  
91120, Palaiseau, France

<sup>b</sup>Ateliers Laumonier, France

Ateliers Laumonier, 11 rue de Chenival - BP 29 - F-95690 Nesles la Vallée, France

<sup>c</sup>IC2MP, Université de Poitiers, France

Université de Poitiers, UMR 7285 CNRS, IC2MP équipe HYDRASA, rue Michel Brunet, Bat. B35, 86073 Poitiers cedex 9,  
France

**Abstract**

A new method has been developed to image surface contamination on-site by short range radiation emitters (such as alpha or beta particle emitters). The measurement is performed in direct contact with the contaminated surface and uses a solid scintillator coupled with Silicon Photomultiplier (SiPM) arrays. The signal readout is processed using a dedicated electronic. The experimental setup used to acquire the data, as well as the analysis procedure, are described and the results are discussed with regard to dismantling requirements. Image reconstruction is investigated using various algorithms. A proof of principle is performed in laboratory using a simple prototype and multiple alpha and beta sources. All the common beta and alpha emitters are detected (including tritium) and tests on gamma radiation are also performed. The minimum detectable activity is estimated to be 0.4 Bq/cm<sup>2</sup> for beta radiations (<sup>14</sup>C) and 0.3 Bq/cm<sup>2</sup> for alpha radiations (<sup>239</sup>Pu). Finally, promising discrimination capability of the prototype is highlighted.

## 34 **Keywords**

35 Dismantling, Autoradiography, Short-range radiation, Contamination imaging

36

## 37 **Abbreviations**

38 SiPM: Silicon PhotoMultiplier

39 CEA: French Alternative Energies and Atomic Energy Commission

40 ASIC: Application-Specific Integrated Circuit

41 FPGA: Field-Programmable Gate Array

42 ADC: Analog to Digital Converter

43

44

## 45 **1 Introduction**

46

47 Characterization of radioactive contamination is a mandatory step of any nuclear facility  
48 dismantling. It is of first importance to detect, locate, and estimate the nature and activity of the  
49 contamination to adapt the dismantling process accordingly [1]. Currently, a large majority of  
50 the characterization is performed using destructive radiochemical methods, which require  
51 sampling from the facility and offline analysis in a dedicated laboratory [2]. While these  
52 methods have good sensitivity, low detection limits, and efficient radioisotopes discrimination,  
53 the issue of the sampling representativeness and the required mathematical models to generate  
54 and estimated map of the contamination at the scale of the facility are complex issues [3].

55

56 As an alternative, several methods to perform measurements directly on-site have been  
57 investigated, most notably for long range radiation [4]. Many projects have developed cameras  
58 capable to image directly gamma (see for example [5, 6, 7]) or neutron radiation (see for  
59 example [8, 9]). Thus, different industrial solutions are currently available commercially.  
60 However, for short-range radiation emitters, such as beta and alpha particles, there is no  
61 industrial solution available for dismantling applications, especially for low contamination  
62 levels. This issue has been chosen by the international community as one of development  
63 needed for the future of contamination characterization [10].

64

65 The main detection difficulty for alpha and beta emitters is related to the high stopping power  
66 of radiation in solid matter. This phenomenon comes from the nature and energy of the charged  
67 particle emitted during the decay process. On the one hand, the typical energy of the alpha  
68 particle encountered in dismantling application ranges from 4 MeV ( $^{232}\text{Th}$  radiation energy 4.01  
69 MeV) to 7 MeV ( $^{252}\text{Cf}$  radiation energy 6.12 MeV) [1]. On the other hand, the typical energy  
70 range for beta particle is from few keV ( $^3\text{H}$  mean radiation energy 5.7 keV) to 2 MeV ( $^{90}\text{Y}$   
71 maximum energy 2.28 MeV). The corresponding thickness of plastic required to stop the  
72 radiation is thus ranging from 25  $\mu\text{m}$  to 60  $\mu\text{m}$  for the alpha emitters and ranging from few ten  
73 of  $\mu\text{m}$  to 1 cm for the beta emitters [11]. Thus, few hundred microns of solid matter between  
74 the decay location and the sensitive part of any contamination monitor is enough to prevent the  
75 detection of short-range emitters. As a consequence, typical contamination monitors used for  
76 dismantling application have a limited sensitivity to short range radiations and are not suitable  
77 to detect low energy beta particle, such as tritium radiation for example.

78

79 Besides the limited sensitivity, most of the contamination monitors do not provide any  
80 information on the localization of the contamination. In practice, the contamination is often  
81 assumed to be homogenous at the scale of the sensitive surface of the detector (several tens of  
82  $\text{cm}^2$ ). If such precision is enough to locate a hot spot at the scale of a facility, it can lead to an  
83 overproduction of waste during the dismantling process. In addition to the limitation on the  
84 precision of the location, traditional contamination monitors are not designed to perform  
85 contamination mapping at the facility scale and do not have any storage capability, requiring  
86 addition of an external system to reconstruct the map of the contamination.

87

88 To tackle this issue, phosphor screen autoradiography has been used with success to provide a  
89 nondestructive but sensitive detection technique capable of imaging short range radiation [12,  
90 13, 14]. Yet, the use of phosphor screens is not suitable for further industrial developments for  
91 dismantling applications due to the exposure time required which is initially unknown and  
92 strongly dependent on the contamination to be investigated. Without any prior knowledge of  
93 the type of radiation expected, each measurement requires typically one day. Therefore, a full  
94 mapping of a facility is highly time-consuming and quite costly since multiple screens need to  
95 be used. In addition, screens are difficult to handle on the field since they require to be handled  
96 in dark environment in order to avoid over-exposure [12].

97

98 More recently, several developments have been made [15, 16, 17] to image alpha or beta  
99 emitters contamination. All these developments present undeniable progress in specific  
100 situation, opening new possibilities for stakeholders dealing with facilities with specific  
101 characterizations. However, none of them provide the overall detection capability of the  
102 existing contamination monitor, easy to handle, robust for industrial processes and capability  
103 of detecting all radiations.

104

105 In this context, the French national radioactive waste management agency (ANDRA) has  
106 funded in 2016 a research project to address the mapping of short range emitters contamination.  
107 The development aims to provide stakeholders with an efficient way to image surface  
108 contamination by short range emitters directly on-site. In this paper, we present the first results  
109 obtained with a laboratory prototype and a field demonstrator.

110

## 111 **2 Laboratory prototype**

112

113 In order to obtain high sensitivity when measuring contamination, a prototype with an active  
114 detection area in direct contact with the potential contaminated solid surface has been  
115 developed. Removing the use of any protective window increases the detection sensitivity,  
116 compared to existing contamination monitors, but brings additional constraints. The surfaces  
117 encountered in dismantling applications can be dirty, rough or even wet, and require a detector  
118 robust enough to be handled in difficult conditions. To meet these requirements, the detection  
119 is based on organic scintillators coupled with SiPM arrays, which were used to collect the light  
120 emitted when a radiation is going through the scintillator. Organic scintillators are widely used  
121 for charged particles detection [18], robust to mechanical constraints and easy to clean. SiPMs  
122 provide high gain amplification (typically  $10^5$ - $10^6$ ), well suited imaging capability with cell size  
123 of few mm<sup>2</sup>, and a small form factor (for a portable detector).

124

125 The performance of this detection principle is investigated through experimental tests  
126 undertaken in CEA laboratory with a first laboratory prototype. The detection system is based  
127 on two independent Hamamatsu S13361-6050 arrays spatially separated by a distance of 21.5  
128 mm. On top of each array can be placed a cylindric BC400 plastic scintillator (1 mm thick, 5

cm diameter) without any use of optical coupling grease/glue. Each S13361-6050 array is composed of 16 independent cells of individual size of 6 x 6 mm<sup>2</sup>. The readout of the 32 channels is performed using a dedicated ASIC, a FPGA and a 12 bits ADC. The prototype was supplied by a Keithley 2450 Sourcemeter® which provides, in addition to the bias voltage, a valuable real time read-out of the current going through the SiPM arrays (typically at the µA level). All the components are enclosed in a hermetic black box to ensure proper light insulation. A picture and a schematic view of the experimental setup are presented in Figure 1. During the experiment, the prototype is connected to a computer using a USB cable and the data acquisition is controlled using a dedicated software developed by the WeeRoc company<sup>1</sup>. To insure stable and reproducible conditions for the measurements, the laboratory prototypes are installed in a room with temperature and humidity monitored at 20°C and 40% respectively. It was noticed, however, that the temperature inside the black box was rising at the startup of the measurement due to the heat dissipation of the electronic components. To minimize the effect of temperature, all the measurements presented in the following work are taken 30 mins after turning the system on, after temperature stabilization.

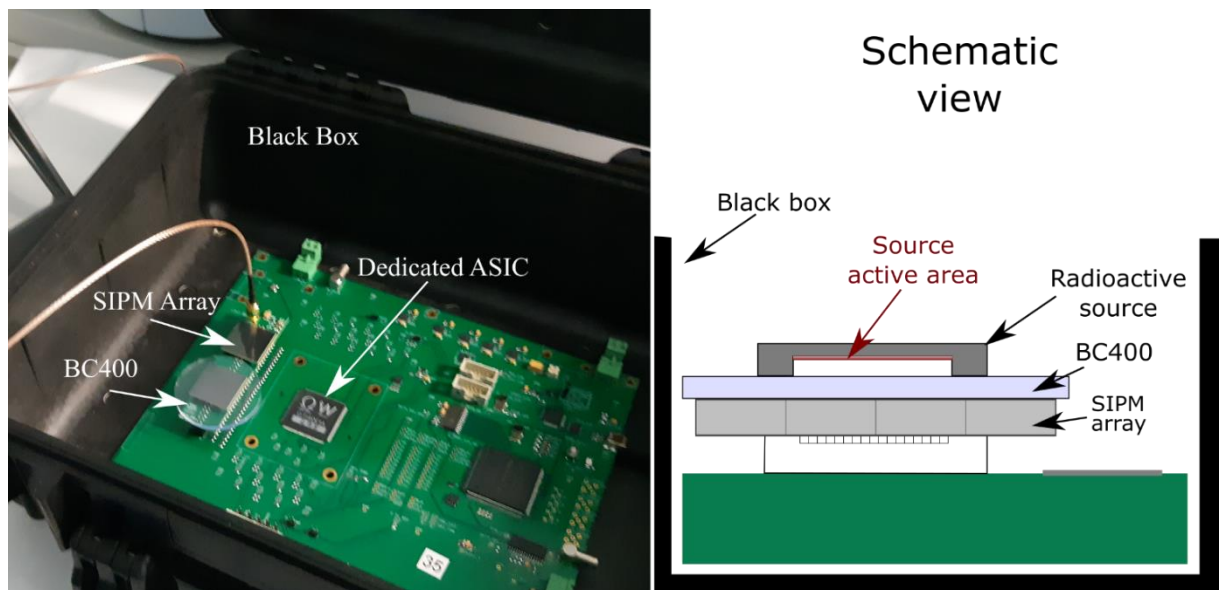


**Figure 1** Left panel is a picture of the first laboratory demonstrator (two SiPM array used, one with BC 400 and one without). The right panel is a schematic view of the same setup (only for the SiPM array covered by the BC400 scintillator).

<sup>1</sup> For more details see <https://www.weeroc.com>

### 151    **3 Prototype operation and calibrations**

152

153    The detection of short-range radiation with the laboratory prototype requires careful adjustment  
154    of several parameters. In particular, the SiPM bias voltage is known to have a strong influence  
155    over the light amplification gain, the detection efficiency and the internal crosstalk of each  
156    SiPM cell (see for example [19]). The detection threshold, i.e. the minimum light intensity  
157    which triggers data recording also plays an important role on counting rate and noise reduction.  
158    The noise counting rate of the SiPM was studied as a function of the threshold for three different  
159    operating voltages. The voltages studied were ranging from the breakdown voltage value  
160    provided by the manufacturer and up to an overvoltage of five volts. The results of the study  
161    are presented in Figure 2. The measurements were performed without any scintillator or  
162    radioactive source, and therefore all detected events were due to the SiPM dark count and  
163    optical cross-talk effect. For a given threshold, the noise frequency is rising by several orders  
164    of magnitude when increasing the bias voltage. Besides, the noise counting rate is falling much  
165    faster, as a function of the threshold value, when decreasing the bias voltage. Since the dark  
166    count cannot be distinguished from real photon detection, it is necessary to set a detection  
167    threshold high enough to minimize the noise counting rate. However, a detection threshold set  
168    too high would strongly lower the detection efficiency of very low energy radiations (which  
169    produce a small number of photons in the scintillator). For optimal performance, the prototype  
170    could therefore be adjusted for each type of radiation and energy. For simplicity purposes  
171    however, a single setting has been used to record the data used in this study. All the  
172    measurements have been performed using a fixed operating voltage equal to 55 V and a  
173    detection threshold corresponding to an equivalent of 12 photons. This relatively low  
174    overvoltage, compared to the 54.5 V breakdown voltage, was chosen in order to maximize the  
175    detection of low energy radiation, such as beta particle coming from tritium. When the  
176    amplitude signal of any of the 32 SiPM (two arrays of 16 SiPM each, see Figure 1) exceeds the  
177    detection threshold, data acquisition triggers and the computer records the corresponding  
178    Analog to Digital Converter (ADC) value of all the 32 SiPMs cells.

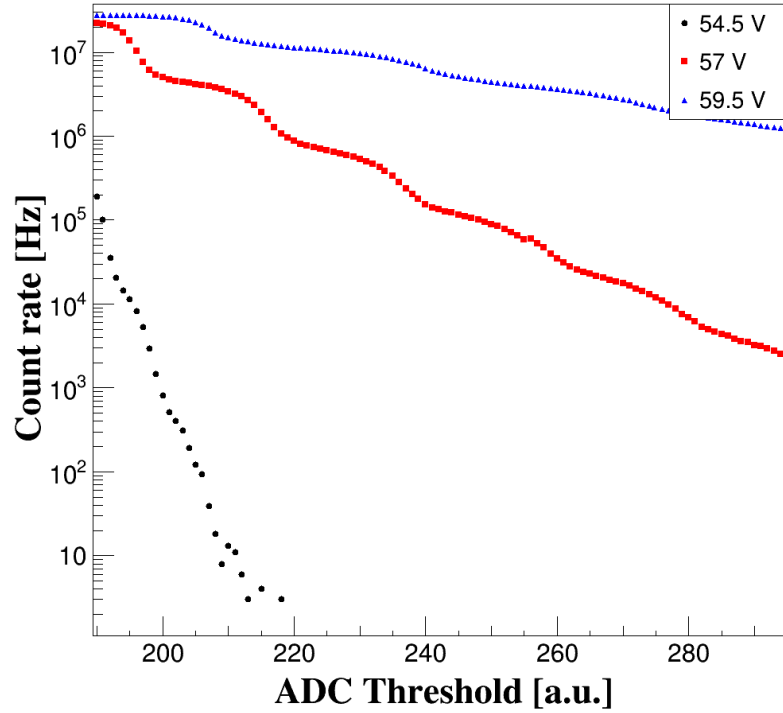


**Figure 2** Evolution of the dark count rate (in Hz) of the prototype as a function of the detection threshold (in arbitrary unit). The study was realized with three different voltages applied to the SiPM: 54.5V (black points), 57V (red squares) and 59.5V (blue triangles).

An SiPM provides an analog output signal with amplitude proportional to the number of electric discharges occurring within the cell. For low and intermediate light intensity this discharge number is proportional to the number of incident photons on the SiPM. For one event, it is therefore possible to calibrate the light intensity in a number of photons detected using the numerical value provided by the ADC through the dedicated ASIC. Each SiPM cell of the prototype is calibrated using a  $^{14}\text{C}$  source, a one millimeter thick BC 400 scintillator and a 10 minutes data acquisition. An example of a raw ADC distribution reconstructed for one cell is presented in Figure 3. The position of each peaks, tagged with red triangles, corresponds to an equivalent number of detected photons. Such positions have been estimated using a gaussian fit. From these positions, the calibration of the ADC value into an equivalent number of photons can be performed, using a linear trend and assuming that the first peak corresponds to one photon equivalent (see insert in Figure 3).

Based on the calibration of all the SiPM cells of the system, the total light intensity detected by the prototype can be reconstructed event by event:

$$L = \sum_i l_i = \sum_i a_i ADC_i + b_i$$

where  $l_i$  is the value of the calibrated light intensity, calculated from the  $ADC_i$  value, corresponding to the SiPM index  $i$  (from 1 to 32) where  $a_i$  and  $b_i$  are respectively the slope and the intercept of the linear calibration.

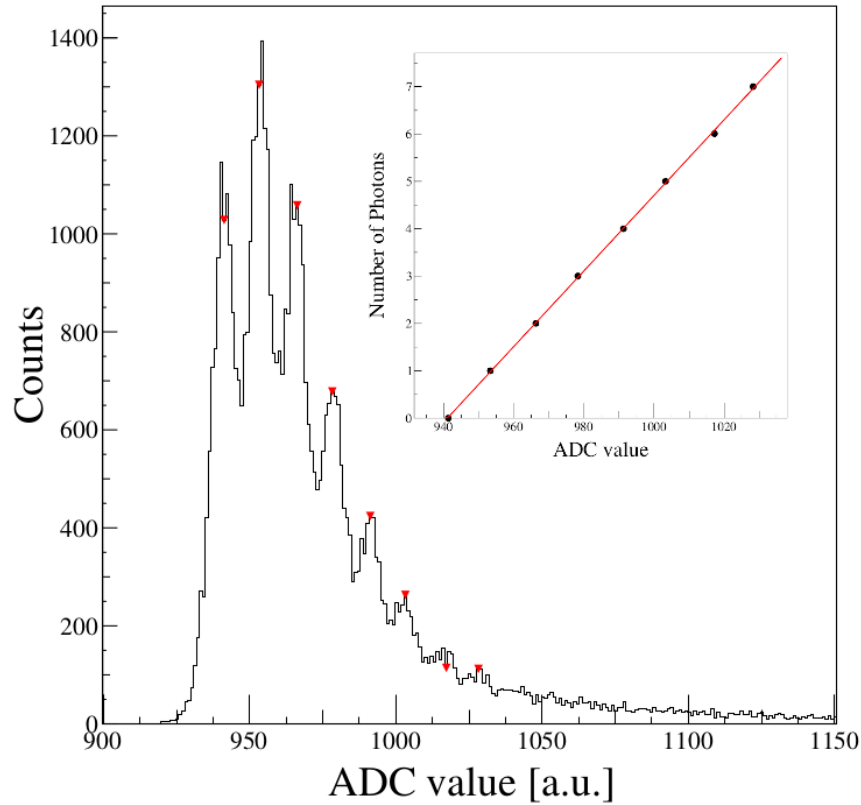


**Figure 3** Distribution of ADC values measured for one SiPM cell of the prototype. The calibration of ADC value in photon equivalent is shown on top right as an insert.

#### 4 Detection characterization

The detection capability of the laboratory prototype is characterized next using the alpha and beta sources presented in Table 1.



213  
214

**Table 1** Properties of the various calibrated alpha and beta sources used for the detector characterization.

Isotope	Radiation emission	Mean radiation energy (keV)	Active surface (mm <sup>2</sup> )	Emerging ( $\alpha$ / $\beta$ ) 2 $\pi$ Activity (Bq)	Surface 2 $\pi$ Activity (Bq/cm <sup>2</sup> )
<sup>3</sup> H	$\beta$	5.7	105	4202 $\pm$ 630	4020
<sup>14</sup> C	$\beta$	49.5	1963	1641 $\pm$ 12	84
<sup>36</sup> Cl	$\beta$	251	908	1634 $\pm$ 12	180
<sup>90</sup> Sr/ <sup>90</sup> Y	$\beta$	196 / 934	2640	1627 $\pm$ 12	62
<sup>239</sup> Pu	$\alpha$ (+ $\beta$ + $\gamma$ )	5139	177	161 $\pm$ 3	92
<sup>241</sup> Am	$\alpha$ (+ $\beta$ + $\gamma$ )	5364	177	121 $\pm$ 2	68
<sup>137</sup> Cs	$\gamma$ + $\beta$	662	2640	178 $\pm$ 10	7

215

216 All these radioisotopes are commonly encountered in dismantling applications and were chosen  
 217 to cover a wide range of energy. These sources are laboratory standards, commonly used for  
 218 calibration purposes, and therefore have a radiation flux certified by the manufacturer. In  
 219 addition, the active areas of the sources are thin surfaces in order to minimize attenuation of the  
 220 radiation energy inside the source material. Finally, the activities of the sources were low  
 221 enough for manual handling and suited to probe the sensitivity of the prototype at a low level  
 222 of contamination. In the specific case of the tritium source, only a mass activity (in Bq/cm<sup>3</sup>)  
 223 was certified by the manufacturer. However, the apparent activity, i.e. number of particles going  
 224 out of the sample by time unit, was required to study the prototype response to radiations. Thus,  
 225 the apparent activity of the source was estimated taking into consideration the attenuation of  
 226 the radiation in the source material using the GEANT4 simulation described in [20, 21]. In  
 227 addition to the alpha and beta sources, one gamma source (<sup>137</sup>Cs), was selected to evaluate  
 228 roughly the response of the prototype to gamma ray emission. Since the <sup>137</sup>Cs source was  
 229 unsealed, the beta particles emitted by the decay were stopped using a 1mm thick aluminum  
 230 foil. The resulting gamma flux was calculated assuming the known branching ratio of the decay  
 231 and the attenuation of gamma rays in the aluminum.

232 During each individual measurement, the alpha and beta sources are put in direct contact with  
 233 the scintillator which is placed on top of one SiPM array (see Figure 1 schematic). The

234 acquisition duration is set to 5 minutes which is a reasonable value for on-site measurement of  
235 facilities being dismantled.

236

#### 237 4.1 Background measurement

238

239 The background level of the prototype is estimated by performing twelve independent  
240 acquisitions over six nonconsecutive days without the use of any radioactive source. For each  
241 of the acquisition, the number of recorded events above the acquisition threshold is determined.  
242 Over all the acquisitions, the number of events spanned from 141 to 301 counts. The counting  
243 rate average is used in the following analyses as the typical background level. The uncertainty  
244 on the background counts is estimated, with a 95% confidence level, using Student's t-  
245 distribution [22]. The background level is thus equal to  $235 \pm 35$  counts for an acquisition of 5  
246 minutes. This corresponds to a relative uncertainty on the background level around 15%. This  
247 represents approximately  $0.8 \pm 0.1$  counts per second for a real time measurement or, taking  
248 into account the prototype detection surface,  $0.14 \pm 0.02$  cps/cm<sup>2</sup>.

249

250 From the background average and associated uncertainty, the Detection Limit of the system can  
251 be estimated, using the Currie formula [23]:

$$252 \quad DL = \frac{-b + \sqrt{b^2 + 4ac}}{2a}$$

253 with

$$254 \quad a = 1$$

$$255 \quad b = -(2k_{1-\alpha}\sigma_0 + k_{1-\beta}^2)$$

$$256 \quad c = (k_{1-\alpha}^2 - k_{1-\beta}^2)\sigma_0^2$$

257 for which

$$258 \quad \sigma_0 = \sqrt{\mu_{BCK} + \sigma_{BCK}}$$

259 Where  $\mu_{BCK}$  is the background level and  $\sigma_{BCK}$  the associated uncertainty. Additionally,  $\alpha$  and  $\beta$   
260 are the expected error probably of false positive counting, respectively false negative counting.  
261 Finally,  $k_{1-\alpha}$  and  $k_{1-\beta}$  are the 1-  $\alpha$ , respectively 1-  $\beta$ , confidence limit interval of the normal

distribution. By taking a false positive and a false negative probability both equal to 5%, the formula can be simplified to:

$$DL = -b + |b|$$

The results of the calculation give a detection limit equal to 259 counts for a 5 minutes acquisition which corresponds to 0.86 count per second for a real time measurement. Taking into account the prototype detection surface, the detection limit is estimated to be equal to 0.17 cps/cm<sup>2</sup>.

## 4.2 Isotope discrimination

Discrimination of the radiation can be performed using the total calibrated light intensity. The distributions obtained with each of the sources were compared to background measurements (performed without any radiation source). The integral of each distribution has been normalized by the emerging activity of the source. The results are presented in Figure 4.

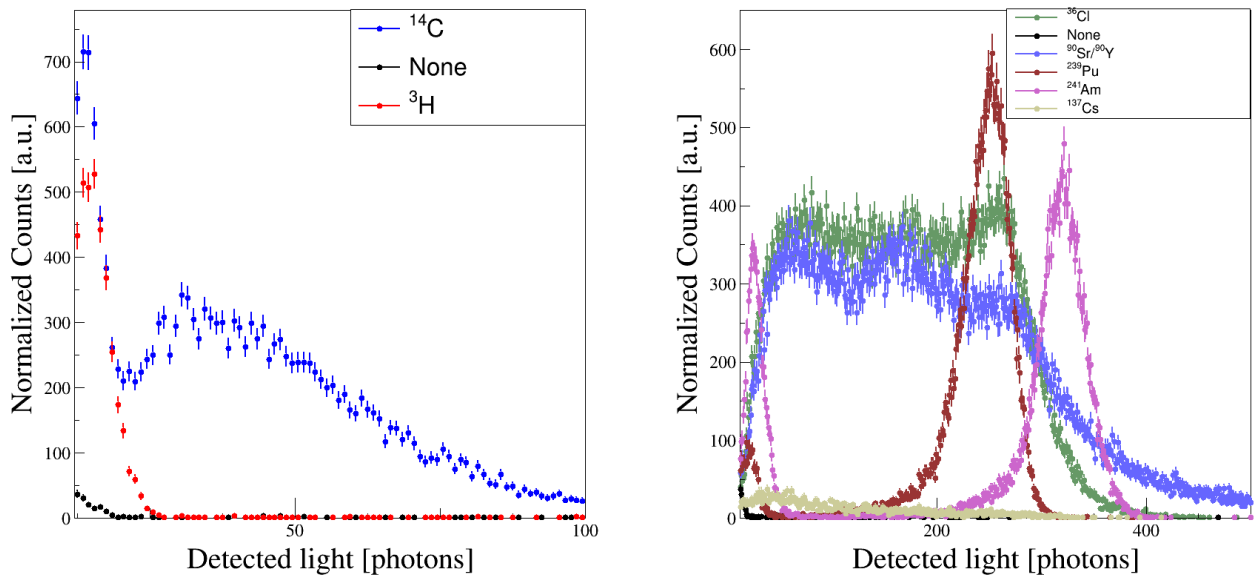


**Figure 4** Reconstructed light distribution obtained for the radioactive sources. The left panel shows the light distribution obtained for <sup>3</sup>H (red) and <sup>14</sup>C (blue), while the right panel shows the light distribution for <sup>36</sup>Cl (green), <sup>90</sup>Sr (dark blue), <sup>239</sup>Pu (dark red), <sup>241</sup>Am (purple), and <sup>137</sup>Cs (light grey). In both cases the distribution obtained without any radiation source is plotted in black.

284 A clear distinction between the alpha and beta sources used can be observed. First, the two  
 285 radiation types exhibit characteristic differences in the reconstructed distribution: the beta  
 286 spectra are large and continuous while the alpha spectra are characterized by narrow peaks.  
 287 Secondly, all the sources could be distinguished from each other based on statistical properties  
 288 of the distributions (such as the average and the standard deviation as display in Table 2). The  
 289 higher the beta particle energy, the higher the number of detected photons (as expected from  
 290 energy loss of the radiation in the organic scintillator [24]). A similar result can be observed for  
 291 the alpha sources, the average number of photons detected for the  $^{241}\text{Am}$  being higher than the  
 292 one measured for the  $^{239}\text{Pu}$  source. This result is very promising in the perspective of identifying  
 293 alpha and beta radiations (more generally performing radiation discrimination) with the  
 294 demonstrator planned to be tested in the future on the field. However, it should be emphasized  
 295 that these preliminary measurements have been performed in laboratory with chemically pure  
 296 sources. In addition, the sources are thin and not affected by the potential matrix effect that  
 297 could be observed for on-site applications (see for example [20, 21]). To confirm this  
 298 preliminary discrimination capability, further analysis has to be performed on actual samples  
 299 and on-site.

300 **Table 2** Number of detected events for a five minutes acquisition, using alpha and beta  
 301 sources of various activities. The statistical estimators were determined from the distribution  
 302 measured for each source.

Isotope	Normalized number of events	Light intensity (photons)	Average light intensity per event (photons)	Light intensity standard deviation (photons)
None	235	$1.56 \cdot 10^4$	59	72
$^3\text{H}$	3731	$8.27 \cdot 10^4$	22	34
$^{14}\text{C}$	37141	$7.47 \cdot 10^5$	42	25
$^{36}\text{Cl}$	102046	$1.71 \cdot 10^7$	168	84
$^{90}\text{Sr}/^{90}\text{Y}$	99336	$1.95 \cdot 10^7$	196	120
$^{239}\text{Pu}$	32724	$7.59 \cdot 10^6$	232	55
$^{241}\text{Am}$	31282	$7.82 \cdot 10^6$	250	122
$^{137}\text{Cs}$	3668	$4.19 \cdot 10^5$	114	79

303

304

### 305 4.3 Detection response linearity

306

307 The counting rate is investigated as a function of source activities by inserting 3 mm thick  
308 plastic collimators between the sources and the plastic scintillator. The study was performed  
309 with  $^{14}\text{C}$  source and  $^{239}\text{Pu}$  source, both presenting homogeneous surface contamination. The  
310 diameters of the collimator aperture were ranging from 1.1 mm to 25 mm. While all nine  
311 different collimators could be used with the  $^{14}\text{C}$  source, only five of them were used with the  
312  $^{239}\text{Pu}$  due to the source size limitation. For each diameter, the expected detection rate was  
313 estimated (see Table 3) assuming homogenous contamination of the source and taking into  
314 account the radiation attenuation between the source and the scintillator. The measurements  
315 were performed three times for each source and collimator and the average counting rate  
316 detected, subtracted from the background counting rate, was determined. The uncertainty on  
317 the counting rate was estimated using the standard deviation of the three measurements and  
318 Student's t-distribution with a confidence interval of 95%. The results obtained are presented in  
319 Figure 5 and in Table 3.

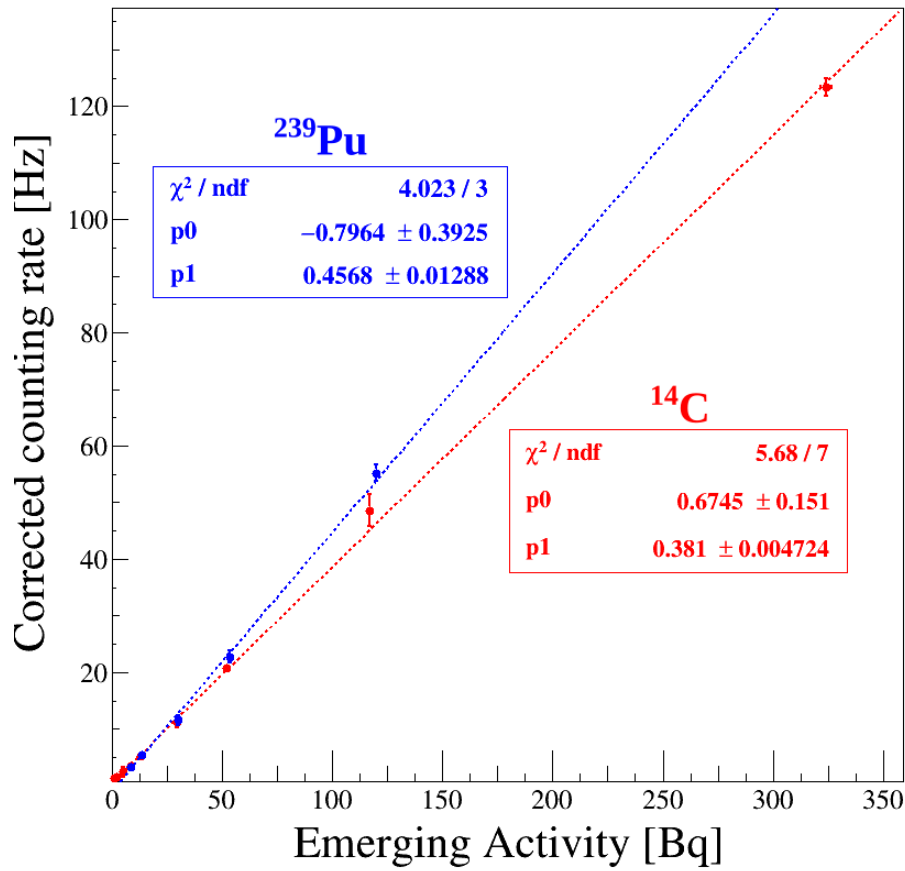


**Figure 5** Study of counting rate of the prototype as function of emerging activity of  $^{14}\text{C}$  (in red) and  $^{239}\text{Pu}$  (in blue) source. The dashed lines are linear fit of the data points. The parameters of the fit are displayed in the insert boxes (p1 is the slope, p0 the intercept)

The data points are fit using linear regression. The coefficients of determination are respectively  $R^2 = 0.999$  for the  $^{14}\text{C}$  and  $R^2 = 0.998$  for the  $^{239}\text{Pu}$ . For  $^{14}\text{C}$ , the linearity is well verified for all the range of activity, except below 8 Hz of detected events for which the prototype overestimates the emerging activity. For the  $^{239}\text{Pu}$  the linearity is verified over all the considered activities. Both for alpha and beta emitter, the detection response is linear enough to perform real time contamination estimation with the field demonstrator to be developed. Due to the low radiation flux coming from the sources, no dead time is observed on the counting rate. Additional studies with higher source activities will be required to investigate further such effect.

**Table 3** Expected and measured counting rates for a 5 minutes acquisition, using both  $^{14}\text{C}$  and  $^{239}\text{Pu}$  sources. The values are presented for various diameters in the masks used to reduce the radiation flux.

Hole diameter (mm)	Expected $^{14}\text{C}$ events rate (Hz)	Measured $^{14}\text{C}$ events rate (Hz)	Expected $^{239}\text{Pu}$ events rate (Hz)	Measured $^{239}\text{Pu}$ events rate (Hz)
1.1	0.6	$1.2 \pm 0.4$	-	-
2	2.1	$1.5 \pm 0.2$	-	-
3	4.7	$2.4 \pm 0.9$	-	-
4	8.3	$3.4 \pm 0.3$	11.5	$8.5 \pm 0.4$
5	13.0	$5.3 \pm 0.7$	17.9	$13.3 \pm 0.7$
7.5	29.2	$11.3 \pm 1$	40.3	$29.9 \pm 0.9$
10	51.9	$20.7 \pm 0.4$	71.6	$53.2 \pm 1.1$
15	116.7	$48.5 \pm 2.9$	161.0	$119.6 \pm 1.5$
25	324.1	$123.4 \pm 1.6$	-	-

#### 4.4 Detection efficiency

The  $2\pi$  detection efficiency  $\epsilon_R$  is an important parameter to quantify the prototype sensitivity to alpha and beta radiations. In particular, a high detection efficiency is to obtain the lowest possible detection limit. The efficiency of the prototype is estimated using the following equation:

$$\epsilon_R = \frac{N - \mu_{BCK}}{\tau A_R} F_R$$

where  $N$  is the number of counts measured during the acquisition time,  $\mu_{BCK}$  is the corresponding background level,  $\tau$  is the acquisition time,  $A_R$  the  $2\pi$  source activity, and  $F_R$  a correction factor to estimate the radiation loss. The latter parameter was introduced in the equation to take into account the radiation attenuation in air located between the source and the scintillator. While the source and the scintillator are in close contact (as in Figure 1), a little space can still generally be observed between the scintillator and the source (except for tritium) due to the supporting frame thickness (typically around 1 millimeter). The attenuation in the air between the two layers is calculated based on a GEANT4 simulation above-mentioned [20, 21].

355 The efficiency of the prototype is calculated for  $^{14}\text{C}$ ,  $^{239}\text{Pu}$ ,  $^3\text{H}$  and  $^{137}\text{Cs}$  source. Taking  
 356 advantage of the previous measurements, the efficiency for  $^{14}\text{C}$  and  $^{239}\text{Pu}$  is determined by  
 357 plotting the counting rate as a function of the emerging activity (reported in Table 3). The slope  
 358 coefficient of the adjusted data, as well as the associated uncertainty, provides the detection  
 359 efficiency for the  $^{14}\text{C}$  and  $^{239}\text{Pu}$ . Regarding  $^3\text{H}$  and  $^{137}\text{Cs}$  sources, using a similar method was  
 360 not possible. For tritium, the collimator would have needed to be very thin to keep a reasonable  
 361 activity (the radiation flux being strongly affected by air). Besides, the relatively small active  
 362 area ( $105\text{ mm}^2$ ) of the source would have required small holes in this thin collimator  
 363 constraining even more the design and construction of such collimator. Regarding the  $^{137}\text{Cs}$ , the  
 364 gamma radiation could have been collimated using lead but the connector used between the  
 365 PCB card and the SiPM arrays can not withstand such heavy load. Instead, a crude estimation  
 366 is performed for both sources using a simple procedure. Three independent measurements are  
 367 recorded and the average of the observed number of detected events is compared to the source  
 368 activity to calculate the efficiency. The uncertainty on the results is estimated using the standard  
 369 deviation and Student's t-distribution with a confidence interval of 95%. The results obtained  
 370 for all the sources are presented in Table 4.

371 **Table 4** Detection efficiency and minimum detectable activity measured with the radioactive  
 372 sources.

Isotope	Radiation	Detection efficiency (%)	Minimum detectable activity (Bq/cm <sup>2</sup> )
$^3\text{H}$	B	$0.15 \pm 0.05$	92
$^{14}\text{C}$	B	$38.1 \pm 0.4$	0.36
$^{239}\text{Pu}$	A	$45.7 \pm 1.3$	0.30
$^{137}\text{Cs}$	$\Gamma$	$6 \pm 1.3$	2

373

374 As a comparison, two industrial contamination portable monitors (commonly used in nuclear  
 375 facilities) are considered: the LB-124 SCINT Series from Berthold technologies [25] and the  
 376 NUHP CoMo-170 from NuviaTech Instruments [26]. According to the manufacturer  
 377 documentations, the typical efficiency is between 14-29% for  $^{14}\text{C}$  and 20 – 45% for  $^{239}\text{Pu}$ . The



deduced efficiencies obtained with the laboratory prototype are comparable to these industrial references, thus proving the validity of the detection principle for dismantling applications. In the cases of  $^3\text{H}$  and  $^{137}\text{Cs}$ , the various experimental constraints and assumptions (performed to calculate the emerging activity) are likely to have a high impact on the deduced efficiency. In particular, the estimations of the uncertainty presented in Table 4 only include the statistical uncertainty but no systemic bias. As a consequence, caution should be taken before drawing conclusions from these estimations. Yet, based on the order of magnitude of the efficiency deduced for both nuclei, preliminary observations can be made. On the one hand, it can be stressed out that these first results are very encouraging for tritium measurements for which no industrial solution can be currently found. On the other hand, the gamma detection efficiency of the prototype seems smaller than the one of the above-mentioned portable monitors. Since the detection was optimized for short range radiations (with a thin organic scintillator), this low efficiency was expected and is not a major flaw. Additionally, a small gamma detection efficiency might provide the possibility to study alpha / beta contamination in facilities with high ambient gamma radiation background.

#### 4.5 Minimum Detectable Activity

Using the previously deduced efficiency, a refined version of the detection limit can be proposed to include the prototype response to the alpha and beta radiations. The estimation is performed for each source using the following formula:

$$MDA_R(\tau) = \frac{DL}{\tau \epsilon_R}$$

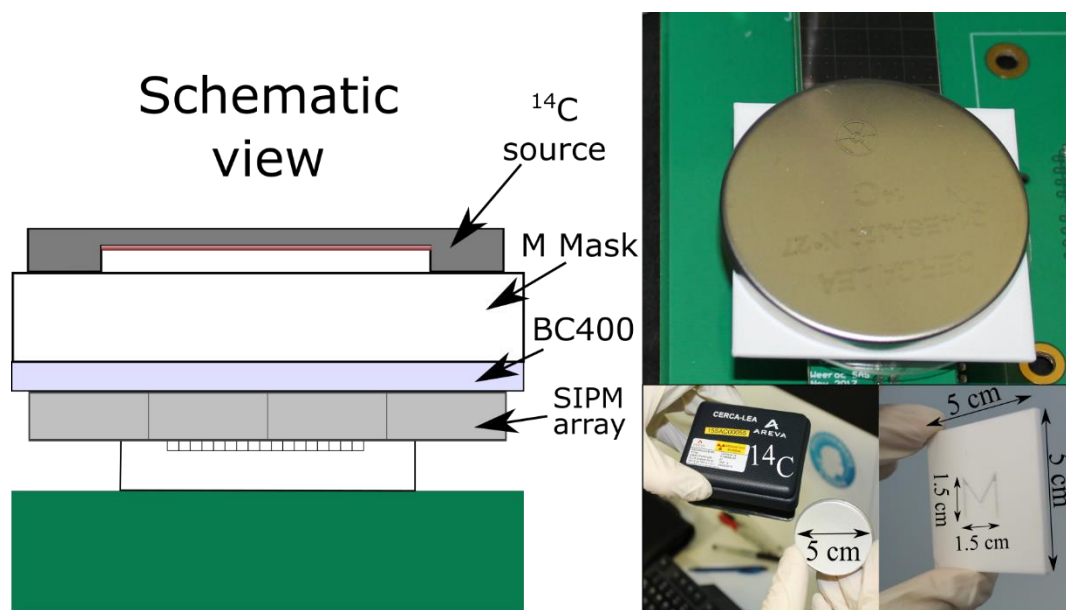
where  $DL$  is the detection limit calculated in the section 4.1,  $\tau$  is the acquisition time considered, and  $\epsilon_R$  is the detection efficiency for the radiation considered. The results obtained with the formula are reported in Table 4. For a typical nuclear facility and for safety purposes, a reasonable threshold used to classify a surface as contaminated is 4 Bq/cm<sup>2</sup> for beta/gamma emitters, 0.4 Bq/cm<sup>2</sup> for alpha and 100 Bq/cm<sup>2</sup> for tritium [27]. The minimum detectable activity obtained with the prototype are of the same order of magnitude for an instantaneous measurement, thus confirming the capability of the prototype to meet the dismantlement requirements.

## 5 Image reconstruction

410

411 Special care has been taken to investigate the image reconstruction capability of the laboratory  
412 prototype. A specific collimator was designed with the letter M carved on it (see right bottom  
413 panel in Figure 6). The size of the M letter in the collimator was 1.5 cm wide by 1.5cm height  
414 and the width of the aperture was 1 mm. The collimator is inserted between the  $^{14}\text{C}$  source and  
415 the scintillator (the associated emerging activity was estimated to be around 43 Bq). A one-hour  
416 acquisition is performed with this configuration using a detection threshold of 12 photons  
417 equivalent for the acquisition. Since the collimator and source are located on the top of one of  
418 the two arrays, only this array was considered for the image reconstruction (4x4 SiPM array).  
419 Two simple algorithms were developed and compared for the reconstruction of the spatial  
420 image of contamination.

421



422

423

424 **Figure 6** The left panel is a schematic view of the setup used to investigate shape  
425 reconstruction of the laboratory prototype. The top right panel is a picture of the setup in  
426 operation and the bottom panels, picture of the  $^{14}\text{C}$  source as well as the M-shape mask.

427

### 5.1 Direct image reconstruction

429

430 The first algorithm, named *triggering cell algorithm*, is based on the number of hardware trigger  
431 occurrences for each SiPM cell. Since these triggers are generated by the dedicated ASIC chip,

they are already contained in the data flux from the system which makes the algorithm easy to implement and to run in real time. From the individual values recorded for the 16 cells of the prototype, a 2D image of the contamination is reconstructed. The image displays in a color scale the number of occurrences for each cell as a function of the horizontal (X) and vertical (Y) positions. In this representation, the size of the pixels corresponds to the geometrical size of the individual SiPM cell (6x6 mm<sup>2</sup>). The result obtained with this algorithm is presented in Figure 7. The color scale (in arbitrary unit) is chosen to enhance the image contrast. The image obtained shows clear counting variation from a pixel to another, ranging from 607 to 3972 counts. This wide range of registered triggers corresponds to the variation of the emerging radiation flux on the investigated surface. However, due to the size of the pixels, the shape of the letter M can barely be distinguished and the obtained shape looks closer to a H capital letter.

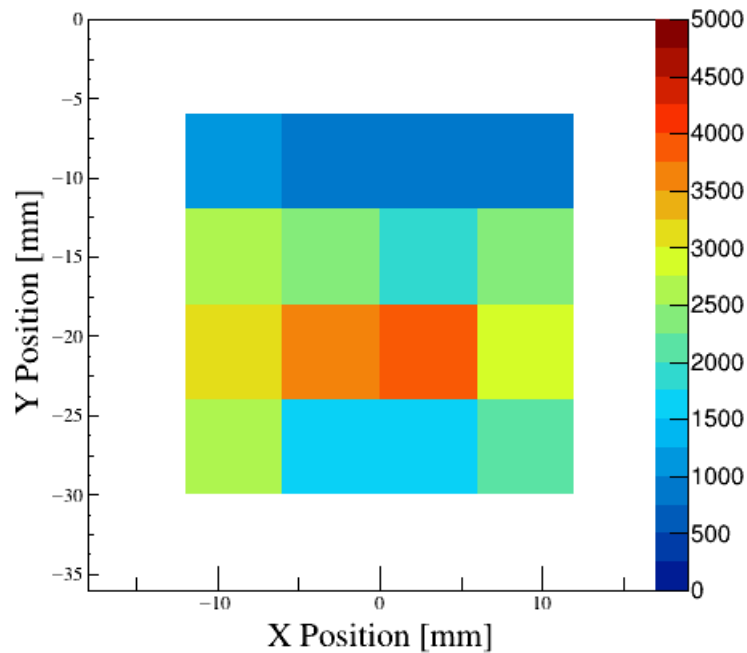
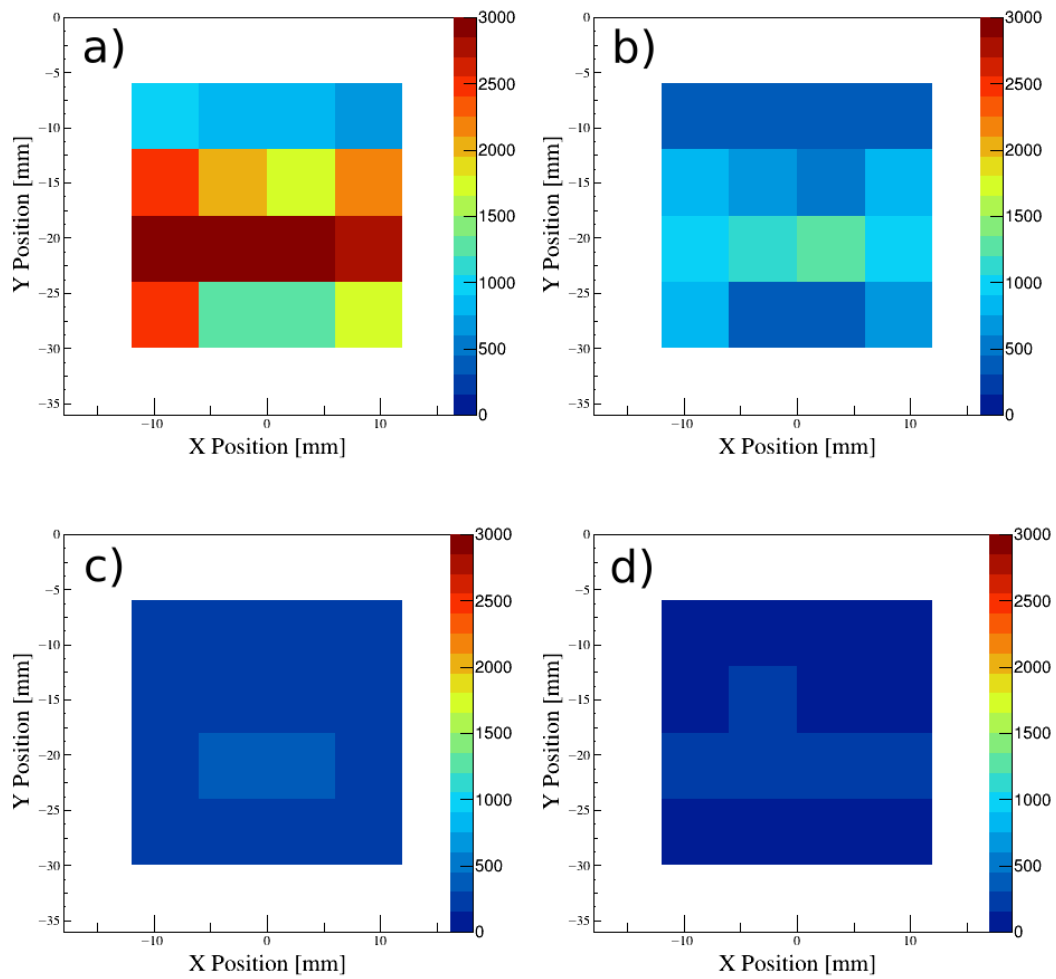


**Figure 7** Spatial reconstruction of the emerging radiation flux of <sup>14</sup>C through a M-shaped collimator using the *triggering cell algorithm*

The influence of the threshold value on the image quality is investigated by performing the reconstruction with different thresholds: 12 equivalent photons, 25 equivalent photons, 50 equivalent photons and 100 equivalent photons. The results obtained are presented in Figure 8. The shape of the letter can be distinguished with low light intensity thresholds but vanished and

451 become homogenous at higher thresholds. As mentioned previously, the light intensity by the  
 452 prototype depends on the energy but also the type of the radiation. Thus, the image  
 453 reconstruction with *triggering cell algorithm* has to be optimized for each type of source. Such  
 454 optimization is not discussed in the present article since only the overall behavior of the  
 455 prototype is discussed.



456  
 457 **Figure 8** Spatial reconstruction of radioactive contamination of  $^{14}\text{C}$  source after a M  
 458 collimator with the *triggering cell algorithm*. The four panels correspond to different  
 459 thresholds: a) to 12 photons, b) to 25 photons c) to 50 photons and d) to 100 photons  
 460

## 461 5.2 Refined image reconstruction

462

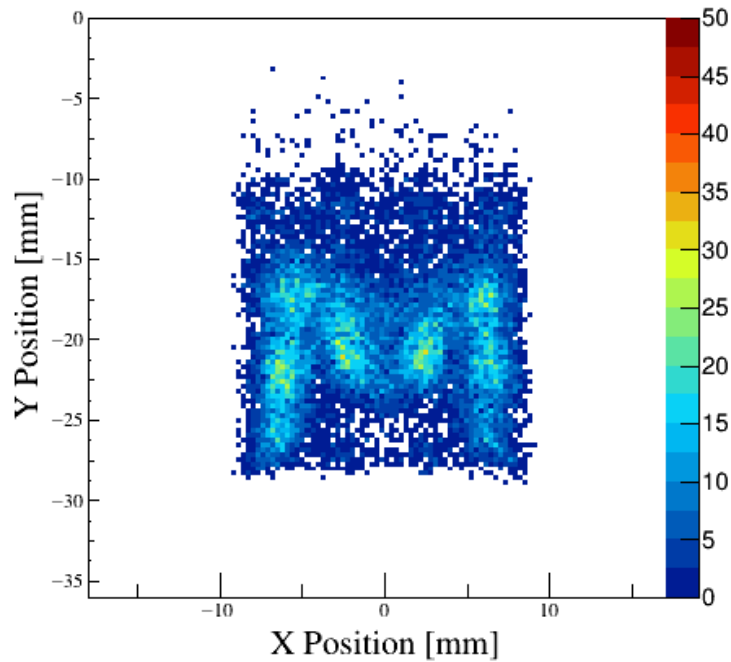
463 A third algorithm, named *weighted average algorithm*, was developed based on the properties  
 464 of the organic scintillator. Since the light is emitted isotropically by the BC400 scintillator along  
 465 the radiation path, the light intensity detected by each cell should be directly proportional to its

geometrical acceptance. Thus, one can have a good approximation of emission position by analyzing the light distribution registered by each cell. For each event, the emission position is reconstructed by performing the following weighted average:

469

$$X_{event} = \sum_i X_i \frac{l_i}{L} \quad Y_{event} = \sum_i Y_i \frac{l_i}{L}$$

where  $(X_i, Y_i)$  and  $l_i$  are respectively the individual center position and detected light of each SiPM and  $L$  the light intensity detected during the event. The distribution of positions deduced for this approach can be plotted in a 2D image for which the pixel size can be reduced compared to the cell dimensions. For comparison purposes, it was chosen to reduce the size of the pixel by a factor 20, i.e. to a size of  $300 \times 300 \mu\text{m}^2$ . The result obtained using this algorithm is presented in Figure 9. Compared to the previous results, the M shape is clearly visible with this third algorithm proving the image reconstruction capability of the prototype.



478

**Figure 9** Spatial reconstruction of radioactive contamination of  $^{14}\text{C}$  source after a M collimator using the weighted average algorithm

481

Finally, the effect of the acquisition duration on image reconstruction quality was studied by performing measurements with 1, 5, 10 and 60 minutes durations. The results, obtained using the weighted average algorithm, are represented in Figure 10. The study clearly shows that the

M shape is not visible after 1 minute, barely appears after 5 minutes but becomes clearly visible after 10 minutes acquisition. These results are a huge progress compared to the existing autoradiography methods which were used previously in dismantlement [12, 13, 14] and for which the phosphor screens were typically exposed to radioactivity for several hours or days.

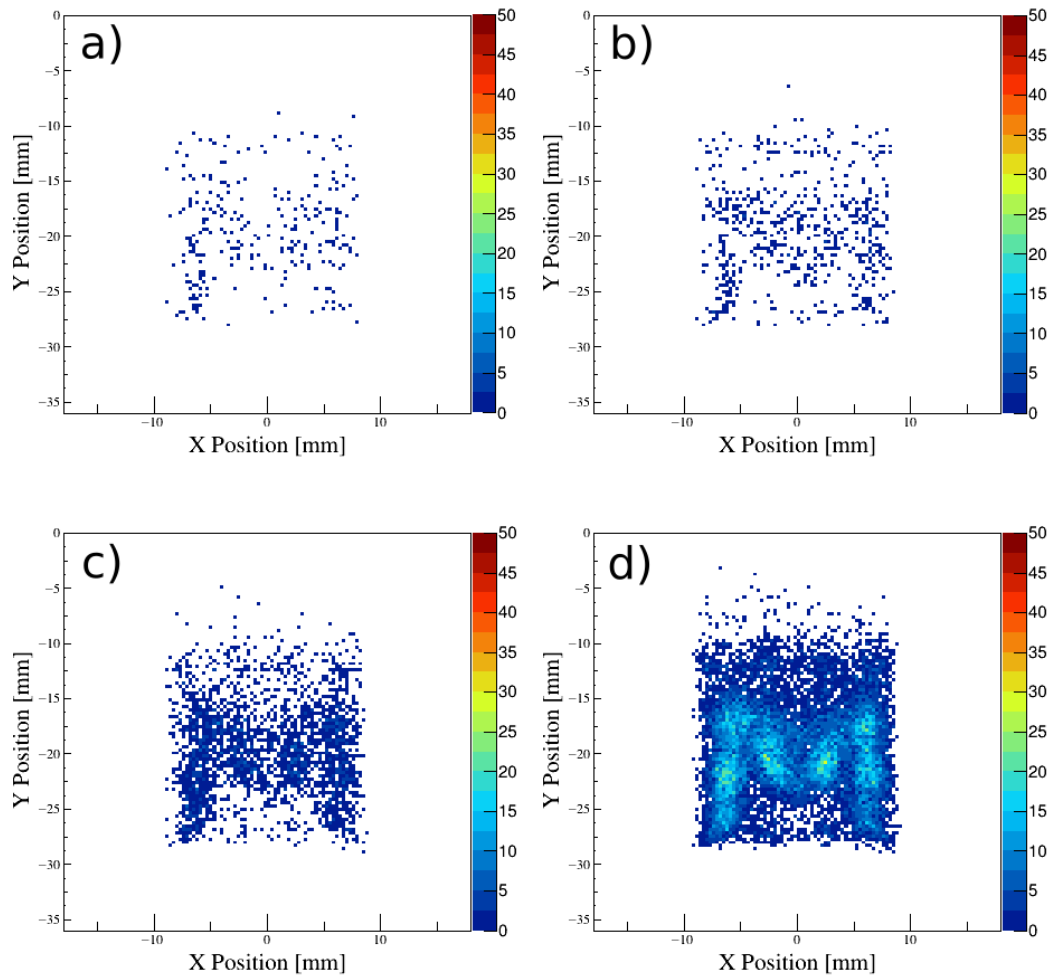


**Figure 10** Spatial reconstruction of radioactive contamination of  $^{14}\text{C}$  source after a M collimator with the Weighted average algorithm. The four panels correspond to different acquisition time: a) 1 minute, b) 5 minutes c) 10 minutes and d) 60 minutes.

### 5.3 Image reconstruction: discussion

Overall, the two tested algorithms have clearly shown the capability of the prototype to distinguish spatial variations of contamination. In the case of the triggering cell algorithm, image reconstructed is rather crude and a clear view of the collimator shape could not be

distinguished due to the intrinsic pixel resolution. Yet, this resolution is already suitable for most cases encountered in dismantling applications where usually several hundreds of square meters are investigated and a precision at the scale of the centimeter is acceptable. Besides, this algorithm already provide a valuable first information if performed in real time and can guide the user on the field. The weighted average algorithm clearly improves the reconstruction of the M shape of the collimator but requires further data processing. The study of the image reconstruction as a function of the acquisition time has shown that even at relatively low level of activity (43 Bq total activity and 84 Bq/cm<sup>2</sup> surface activity of <sup>14</sup>C) about 5 to 10 minutes of acquisition is enough to provide a first image of the contamination. Finally, if the two algorithms used in this work are enough to investigate image reconstruction capability of the prototype, literature is widely available for pixel-based detectors (see for example [28, 29]). Therefore, if required by the application, further improvements can be foreseen with the prototype.

## **7 Development of an industrial demonstrator**

Based on the experience gathered with the laboratory prototype, a first industrial demonstrator was developed in collaboration with the Laumonier company<sup>2</sup>. The demonstrator is designed with a larger sensitive area, using four Hamamatsu S13361-6050, for a final spatial detection of 5x5 cm<sup>2</sup> (see Figure 11). A new electronic, based on the same ASIC and FPGA as the initial prototype, is designed to handle the readout of the 64 channels simultaneously. Specific plastic scintillators, squared 5.5x5.5 cm<sup>2</sup> and 3 mm thick, were used to fully cover all the sensitive surface of the SiPM arrays. The demonstrator is mainly developed to analyze samples coming from facilities undergoing dismantling but also to perform measurements directly on-site (for example on walls or floors). As a consequence, the device is designed to be portable and with a power battery to provide autonomy in the field. A dedicated software has been developed by the Laumonier company to perform online setup, operation, and image reconstruction directly on the field. Finally, to insure a proper light insulation during the measurement a specific rubber ring is designed to be place under the demonstrator cover. Optimization of the software,

---

<sup>2</sup>Ateliers Laumonier :. <https://www.at-laumonier.fr/>

528 handling and light shielding is still ongoing at the Laumonier company but preliminary tests  
529 were performed in laboratory.



530

531

**Figure 11** First demonstrator developed in collaboration with  
the Laumonier company.

532

533

534 Investigation of the demonstrator image reconstruction is performed with two samples:

535

- A core sample from concrete contaminated on surface by  $^{238}\text{U}$  (depleted Uranium). Beforehand, the sample activity was estimated using standard alpha spectrometry. The spatial contamination was estimated to be around  $0.8 \text{ Bq/cm}^2$  for a total activity of  $5 \text{ Bq}$ .
- A tungsten sample which was prepared during the TRANSAT project [30]. The sample is contaminated by tritium gas and its activity was estimated around  $200 \text{ MBq}$  on the whole surface of the sample. This value is determined after a destructive measurement of the sample after demonstrator measurements. The stability of the sample contamination was controlled in laboratory before measurements.

536

537

538

539

540

541

542

543

544

545

Contrary to the prototype, for which calibrated sources were used, it was chosen to test the demonstrator with field type sample in order to have measurement conditions similar to industrial applications.

546

547

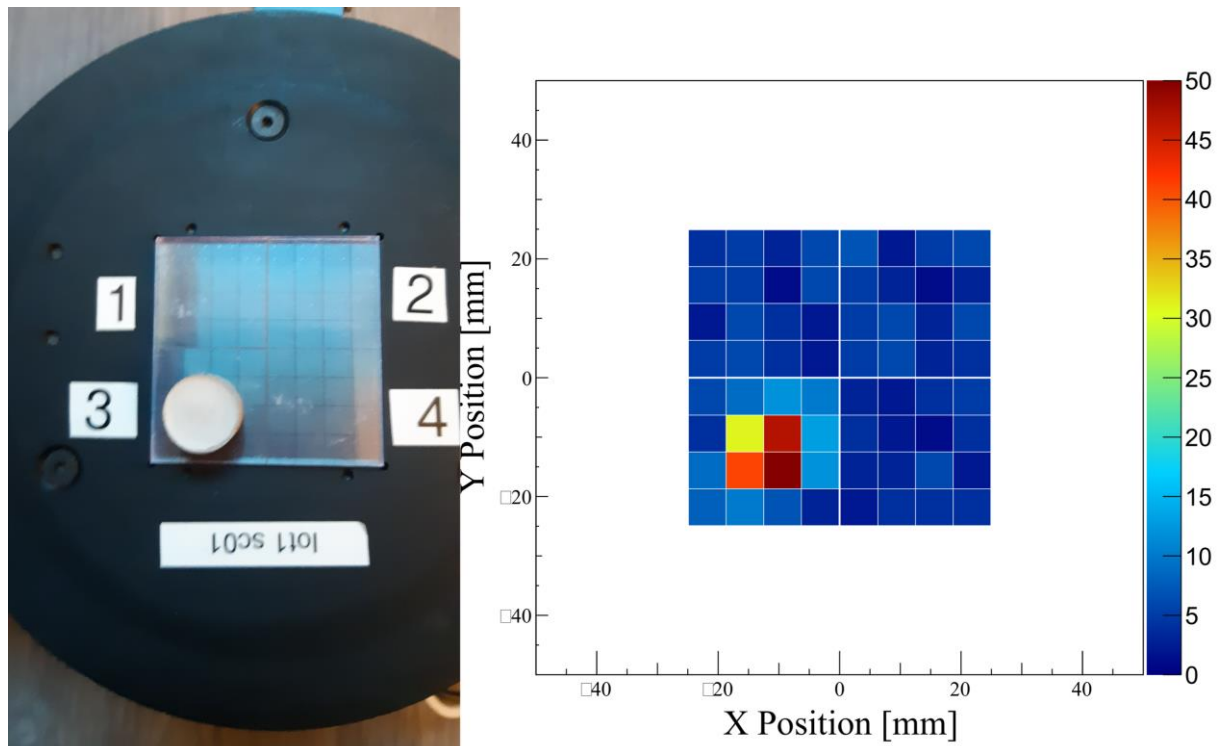
548

549

For both samples, several measurements are performed with the demonstrator during a three minutes acquisitions and using a  $55 \text{ V}$  bias voltage on the SiPM arrays (similar to the voltage used with the laboratory). The measurements are undertaken in the same laboratory as the prototype with similar temperature and humidity conditions. For each measurement, a



550 *triggering cell algorithm* is used to reconstruct the demonstrator contamination image. In both  
551 cases the detection threshold was tuned to increase the image contrast.



552  
553 **Figure 12** Measurement with the industrial demonstrator of a concrete core sample  
554 contaminated with Uranium

555 Regarding the concrete sample, the demonstrator was able to reconstruct properly the position  
556 of the sample (example displayed in Figure 12). Given the low contamination of the sample,  
557 this preliminary result is very promising for various facilities undergoing dismantlement in  
558 France which require alpha contamination mapping.

559 Similarly, encouraging results are obtained with the tungsten sample. The image of the sample  
560 could be reconstructed for several positions (example displayed in Figure 13). Contrary to the  
561 previous concrete sample, mostly one single cell was triggering the acquisition. This could be  
562 easily explained by the geometrical shape of the sample and the very short range of the tritium  
563 radiation. Detecting tritium contamination with a portable device is always a challenge and  
564 these preliminary results are thus very encouraging for the development of the demonstrator.

565 As a comparison, several acquisitions are also performed also without the use of any radioactive  
566 source. For each of this background acquisition, the reconstructed image was homogenous with  
567 very low count rate on each of the SiPM cells. .

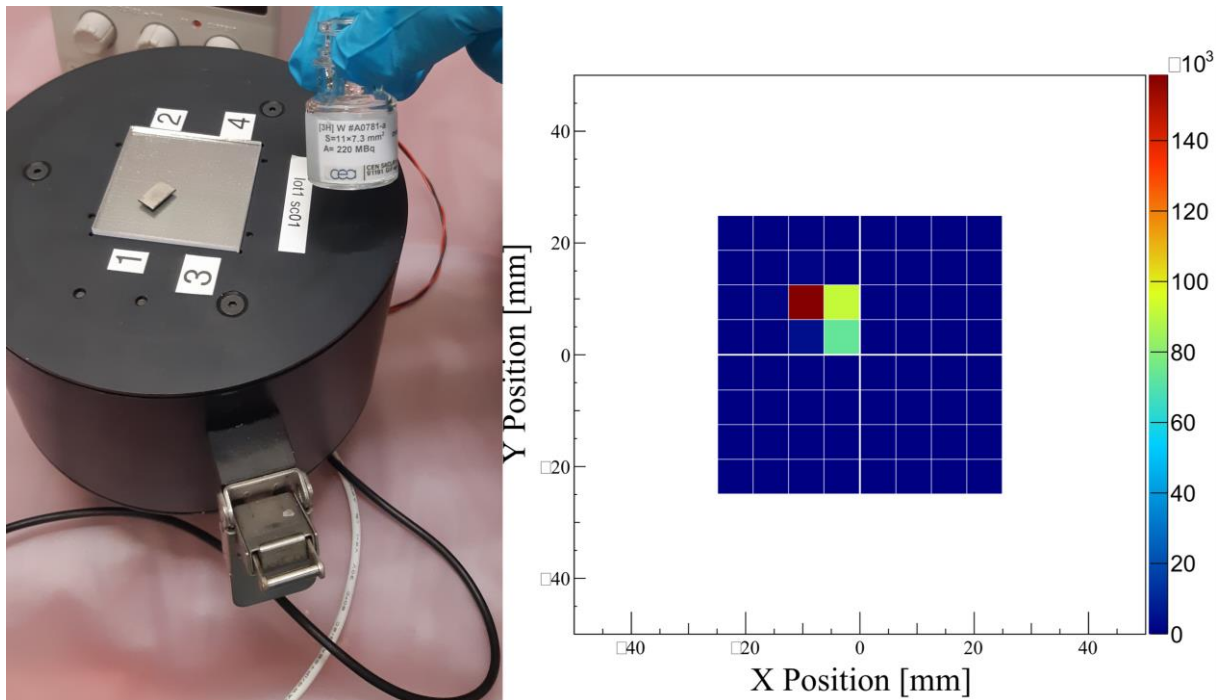


**Figure 13** Measurement of a concrete core sample contaminated with the industrial demonstrator

The demonstrator is currently being tested directly in various facilities in France. The experience gathered in laboratory and in the field should provide very valuable data for the development of an industrial contamination detector.

## 8 Conclusion

The preliminary development of an alpha / beta camera for dismantling applications has been performed. A first prototype has been constructed with 32 SiPM cells of  $6 \times 6 \text{ mm}^2$  coupled to organic scintillators and associated with an electronic readout based on a dedicated ASIC. The prototype has been tested with alpha and beta sources commonly encountered in dismantlement and has shown promising detection results: good beta and alpha detection efficiency, direct tritium detection, relevant Minimum Detectable Activity for common radioisotopes, linear response with activity and crude radiation discriminations. Additionally, the image reconstruction performed with various algorithms has confirmed the position sensitivity of the prototype within a reasonable acquisition time.

An industrial demonstrator, with an improved sensitive area ( $5 \times 5 \text{ cm}^2$ ), was designed and constructed in collaboration with a French company based on the laboratory prototype first results. The preliminary analyses performed with the demonstrator validate the capability of the

588 technology. With additional development and refinement the development could lead to  
589 commercialization of alpha / beta detector for dismantling applications.

590

## 591 **Acknowledgments**

592 This work was performed within the Investments for the future program of the French  
593 Government and operated by the French National Radioactive Waste Management Agency  
594 (Andra). The authors want to acknowledge the support provided by WeeRoc company regarding  
595 the operation of the dedicated ASIC. Finally, S. Leblond would like to express his gratitude to  
596 C. Querré and N. Aychet for the technical support in the collimators design.

597

## 598 **References**

- 599 [1] International Atomic Energy Agency (2017) Radiological Characterization from a Waste  
600 and Materials End-State Perspective: Practices and Experience, OECD  
601
- 602 [2] Pérot B et al. (2018), The characterization of radioactive waste: a critical review of  
603 techniques implemented or under development at CEA France, European Physical Journal  
604 Nuclear Sciences & Technologies, 4: 1-24  
605
- 606 [3] International Atomic Energy Agency (2013) Radiological characterization for  
607 Decommissioning of Nuclear Installation, OECD  
608
- 609 [4] International Atomic Energy Agency (2017) In Situ Analytical Characterization of  
610 Contaminated Sites Using Nuclear Spectrometry Techniques, Analytical Quality in Nuclear  
611 Applications Series 49  
612
- 613 [5] Iltis A et al. (2018) Temporal Imaging CeBr 3 Compton Camera: A New Concept for Nuclear  
614 Decommissioning and Nuclear Waste Management, European Physical Journal Web of  
615 Conferences, 170: 1-5  
616
- 617 [6] Sato Y et al. (2018) Remote radiation imaging system using a compact gamma-ray imager  
618 mounted on a multicopter drone, Journal of Nuclear Science and Technology, 55: 90-96  
619
- 620 [7] Amoyal G. et al. (2020) Development of a hybrid gamma camera based on Timepix3 for  
621 nuclear industry applications, Nuclear Instruments and Methods in Physics Research Section  
622 A: Accelerators, Spectrometers, Detectors and Associated Equipment, 9: 164838  
623
- 624 [8] Pang X et al. (2019) A compact MPPC-based camera for omnidirectional ( $4\pi$ ) fast-neutron  
625 imaging based on double neutron–proton elastic scattering, Nuclear Instruments and Methods

626 in Physics Research Section A: Accelerators, Spectrometers, Detectors and Associated  
 627 Equipment, 944: 162471  
 628  
 629 [9] Kamiya Y et al. (2020) Development of a neutron imaging sensor using INTPIX4-SOI  
 630 pixelated, Nuclear Instruments and Methods in Physics Research Section A: Accelerators,  
 631 Spectrometers, Detectors and Associated Equipment, 979: 164400  
 632  
 633 [10] International Atomic Energy Agency (2014) R&D and Innovation Needs for  
 634 Decommissioning Nuclear Facilities, OECD  
 635  
 636 [11] Bergeret M J al. (2005) ESTAR, PSTAR, and ASTAR: Computer Programs for  
 637 Calculating Stopping-Power and Range Tables for Electrons, Protons, and Helium Ions, NIST  
 638 Standard Reference Database 124  
 639  
 640 [12] Fichet P et al. (2012), Tritium analysis in building dismantling process using digital  
 641 autoradiography, Journal of Radioanalytical Nuclear Chemistry, 291: 869–875  
 642  
 643 [13] Leskinen A et al. (2013) Digital autoradiography (DA) in quantification of trace level beta  
 644 emitters on concrete, Journal of Radioanalytical Nuclear Chemistry, 298:153–161  
 645  
 646 [14] Haudebourg R et al. (2015) A non-destructive and on-site digital autoradiography-based  
 647 tool to identify contaminating radionuclide in nuclear wastes and facilities to be dismantled,  
 648 Journal of Radioanalytical Nuclear Chemistry, 309: 551–561  
 649  
 650 [15] Morishita Y et al. (2017) Flexible alpha camera for detecting plutonium contamination,  
 651 Radiation Measurements, 103: 33-38  
 652  
 653 [16] Kim J et al. (2018) Feasibility of miniature radiation portal monitor for measurement of  
 654 radioactivity contamination in flowing water in pipe, Journal of Instrumentation, 13: 1022-1022  
 655  
 656 [17] Morishita Y et al. (2017) Flexible alpha camera for detecting plutonium contamination,  
 657 Radiation Measurements, 103: 33-38  
 658  
 659 [18] L'Annunziata M (2020) Handbook of Radioactivity Analysis Volume 1: Radiation Physics  
 660 and Detectors, 4th ed, Academic Press  
 661  
 662 [19] Klanner R (2019) Characterisation of SiPMs, Nuclear Instruments and Methods in Physics  
 663 Research Section A: Accelerators, Spectrometers, Detectors and Associated Equipment, 926  
 664 36-56

665

666 [20] Billon S et al. (2019) From Bq cm<sup>-3</sup> to Bq cm<sup>-2</sup> (and conversely)—part 1: a useful  
667 conversion for autoradiography, *Journal of Radioanalytical Nuclear Chemistry*, 320: 643–654  
668

669 [21] Billon S et al. (2019) From Bq cm<sup>-3</sup> to Bq cm<sup>-2</sup> (and conversely)—part 2: useful dataset  
670 to apply the conversion to decommissioning operations, *Journal of Radioanalytical Nuclear*  
671 *Chemistry*, 320: 699–709  
672

673 [22] Walpole R E et al. (2006) *Probability & Statistics for Engineers & Scientists*, 7th ed, John  
674 Wiley & Sons Inc, Pearson  
675

676 [23] Kirkpatrick J M et al. (2013) Minimum detectable activity, systematic uncertainties, and  
677 the ISO 11929 standard, *Journal of Radioanalytical Nuclear Chemistry*, 296: 1005-1010  
678

679 [24] Knoll G, *Radiation Detection and Measurement*, 4th edition (2010) John Wiley & Sons  
680 Inc, Verlag  
681

682 [25] Berthold, LB 124 SINCT contamination monitor, available at  
683 [https://www.berthold.com/en/radiation-protection/products/contamination-monitors/alpha-](https://www.berthold.com/en/radiation-protection/products/contamination-monitors/alpha-beta-gamma-measurement-lb-124-scint/)  
684 [beta-gamma-measurement-lb-124-scint/](https://www.berthold.com/en/radiation-protection/products/contamination-monitors/alpha-beta-gamma-measurement-lb-124-scint/) Accessed on June 18th, 2021  
685

686 [26] *NUVIATECH Instruments*, Specification sheet CoMo-170/300, available at  
687 <http://www.nuviatech-healthcare.com/product/hand-held-contamination-monitor/> Accessed on  
688 June 18th, 2021  
689

690 [27] *United Nations Economic Commission for Europe*, International Carriage of Dangerous  
691 Goods by Road, Volume I: Agreement and Protocol of Signature 2019 ed, available at  
692 [http://www.unece.org/trans/danger/publi/adr/adr\\_f.html](http://www.unece.org/trans/danger/publi/adr/adr_f.html) Accessed on June 18th, 2021  
693

694 [28] Esposito M et al. (2011) Energy sensitive Timepix silicon detector for electron imaging,  
695 *Nuclear Instruments and Methods in Physics Research Section A: Accelerators, Spectrometers,*  
696 *Detectors and Associated Equipment*, 652: 458-461  
697

698 [29] Gehrke T et al (2018) Theoretical and experimental comparison of proton and helium-  
699 beam radiography using silicon pixel detectors, *Physics in Medicine & Biology*, 63: 035037  
700

701 [30] Bernard E et al (2019) Tritium retention in W plasma-facing materials: Impact of the  
702 material structure and helium irradiation, *Nuclear Materials and Energy*, 19: 403-410